Research Article

Multi-modal Sensing Soft End-Effector for Underwater Applications

Liam B Cross, Rafsan Al Shafatul Islam Subad and Kihan Park*

Department of Mechanical Engineering, University of Massachusetts Dartmouth, USA

*Corresponding author: Kihan Park, Department of Mechanical Engineering, University of Massachusetts Dartmouth, Dartmouth, MA02747, USA

Abstract

The underwater domain of soft robotic end-effector development is an emerging field that calls for advancements to multi-modal sensing solutions in order to achieve a wide fluctuation of conformable object manipulation. In this paper, the design of a 3-digit end-effector capable of 6 degrees of shape sensing and 12 points of force sensing is proposed. Integral to the end-effector's design is the presentation of its waterproofed soft-robotic actuators, each capable of 2-point shape sensing and 4-point force sensing. The individual actuator is designed as a uni-directional, bellow-type, PneuNet actuator built from silicone material. On-board sensors utilize widely available piezo-resistive components which allow the actuator to act as a low-cost entry to shape sensing and force sensing. Each actuator exhibits a 2-part compound radius flex-sensor array and a 4-part single-point force sensor array. Of unique design is the bellow-type actuator's custom chamber layout which gives it the ability to resemble approximated closed curvature of a human pointer finger. A technique for shape reconstruction is presented that estimates the shape of the soft actuator based upon embedded flex sensor measurements. The actuator is interrogated under transient pressure range to examine its grasp performance, shape sensing, and force measuring capabilities. The actuator is tested as a stand-alone unit, tested in tandem with a secondary unit, and also equipped with the proposed 3-digit end-effector. Each actuator and servo motor are subjected to an underwater ground-fault test to examine preliminary electrical integrity when submerged below surface level water, whereas visual inspection of a single 3-digit grasp is performed on a cylindrical object under surface level water. The overall goal of this work is to exhibit a tangible design solution for waterproofed multi-modal sensing within the soft robotic design frame for various underwater robotic applications.

Keywords: Soft Robotics; Three-finger Gripper; Low-cost Shape Sensing; Multi-modal Sensing; Underwater Applications

Introduction

Robotic end-effectors have served to play an essential role in the manipulation of remote objects for both land-based and underwater operations during the last two decades [1]. Typical end-effector technologies utilized in these missions have been conditioned by human remote-control assisted by camera vision, whereas mechanical systems have been regularly characterized by solid-body rigid mechanics. With recent developments in soft robotic technologies and multi-modal sensing, there is a promising outlook for robotic manipulator platforms to conform to soft robotic continuum mechanics featuring multi-modal sensing capabilities. The next generation of robotic manipulators will feature soft-material construction equipped with embedded multi-modal sensing capability not only to provide additional in- formation to an operator but also to enhance the level of tasks that a robot can complete autonomously [2,3]. Soft-material end-effectors will enable robots to conduct more complex tasks that have not yet been achievable by conventional rigid robots [4,5]. Moreover, embedded capabilities of shape sensing and force measurement will allow for soft robots to identify objects that are handled while working in harsh environments unable to utilize camera vision.

Regarding soft robotic technologies that have been implemented in the underwater environment, there are a handful of robust solutions that provide novel approaches to grasping and manipulating objects [6]. Calisti et al. and Cianchetti et al. have reported on a soft, eight-armed octopi's robot that is capable of grasping soft objects like jellyfish [7,8]. However, even though the eight-armed robot is able to achieve an impressive degree of freedom (DOF) in actuation it has rarely been validated in practical underwater ocean testing. Alternatively, Licht et al. presented a partially filled jamming gripper for underwater recovery of objects resting on the seafloor [9]. The end-effector proved effective in obtaining smaller objects, though there is no evidence that it

has been tested grasping larger objects. Furthermore, two main predecessor end-effectors that have inspired the design concepts introduced in this technology review are a 3-digit, bellow-type end-effector presented by Kurumaya et al. used for cultivating sea- animals at shallow depths up to 30 m [10], as well as a 4-digit, bellow / boa-type configurable actuator presented by Gallaway et al. used for sampling of a deep-sea reef which was tested at depths up to 800 m [11].

The following Materials and Methods section will provide a high-level overview of the design intent behind the 3-digit end-effector proposed in this technology review. A breakdown of the end-effector's actuator will be provided to exhibit its 3-tiers of capabilities: pneumatic actuation [12], shape sensing [13], and force sensing. To understand the actuator's grasp mechanics, critical geometric considerations for custom PneuNet chamber layout and varying chamber wall thickness will be explained. Following the design intent of the end-effector and its actuators will be a qualitative review of force sensor calibration and a shape sensing algorithm implemented in this study. The Results and Discussion section will follow in-suite to discuss the quality of data collected pertaining to mono-actuator, dual-actuator, and tri- actuator operation as seen on the 3-digit end-effector. The sequence of experimental tests will interrogate curvature approximation based upon the full range of actuator motion, force sensing data collected during object grasping, grasping-modes of dual-actuator operation, as well as shape reconstruction pertaining to tri-actuator operation on the 3-digit end-effector. A preliminary waterproof test will be implemented as an underwater ground-fault test to verify the electrical integrity of each actuator and servo motor when submerged within water, whereas a visual will be provided to exhibit the 3-digit end-effector's performance when fully submerged within water. The Conclusion section will close out this technology review by summarizing the quality of information presented, highlighting the novelty of the work, and providing an outlook toward the future scope of design.

Materials and Methods

Design Intent

The end-effector proposed in this technology review is designed as a waterproofed 3-digit end-effector capable of twelve points of force recognition with six degrees of shape sensing. Each actuator, or finger, is a uni-directional PneuNet actuator featuring four piezo-resistive single-point force sensors capable of gathering tactile force data and two piezo-resistive flex sensors capable of gathering curvature data to approximate compound radius curvature. Pressure sensing is utilized in conjunction with a pneumatic control system to monitor and limit the internal pressure of each PneuNet actuator. The end-effector's actuators feature bi-directional rotational freedom of $\pm 60°$, or a total of $120°$, allowing the end-effector to grasp both spherical and cylindrical objects. Rotational freedom is achieved via waterproof servo motors stationed behind each actuator and sitting within a bearing-block interface. The bearing-block interface features a modular front-loaded spline design for easy actuator and servo interchangeability, and easy serviceability to the bearing block. The sensors used in this end-effector are low-cost, off- the-shelf components enabling a low-cost entry, functional design solution for underwater tactile force and shape sensing. The implemented force sensor (Flexiforce A-201 Sensor, Tekscan, USA) is a single- point, piezo-resistive sensor with a range of 0 - 4.4 N. The implemented shape sensor (FS-L-0055- 253-ST, Spectra Symbol, USA) is a piezo-resistive flex sensor with an active length of 55.4 mm. The implemented pressure sensor (HSCDANN100PGAA5, Honeywell, USA) is a single-axial sensor capable of roughly 689.5 kPa pressure range. Figure 1 is an overview image of the end-effector's complete design.
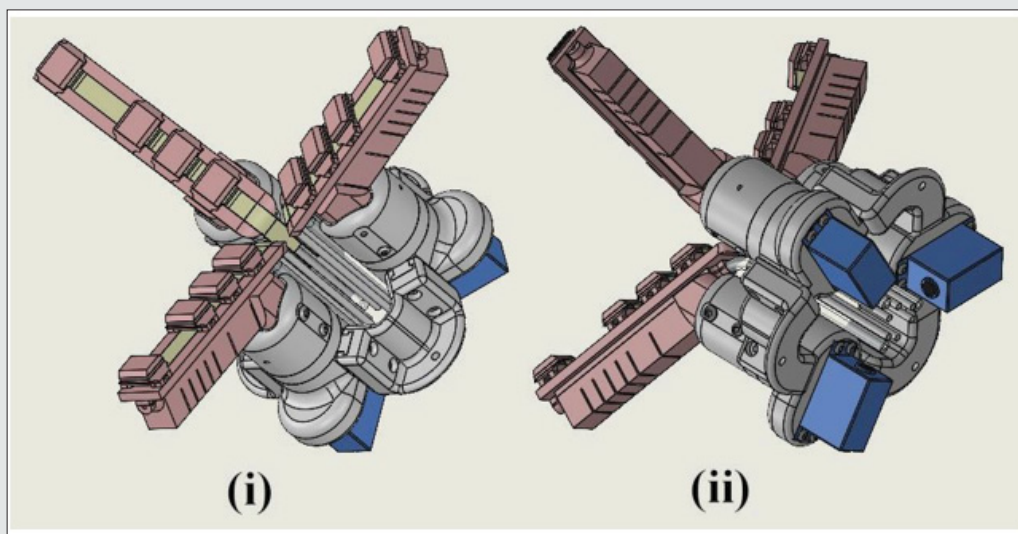

Figure 1: 3D models of the proposed 3-digit end-effector: (i) front view and (ii) back view.

3-tier Actuator Design

Each actuator features a 3-tier design approach as shown in Figure 2 to characterize the pressure vessel, shape sensing layer, and force sensing layer in one complete package. In the actuator's current design phase each tier is bonded together using Sil-Poxy silicone adhesive for experimental performance testing. However, the long-term design goal is for each tier to be separable and interchangeable allowing for actuators to be optimally serviced pertaining to material lifetime and sensor performance.
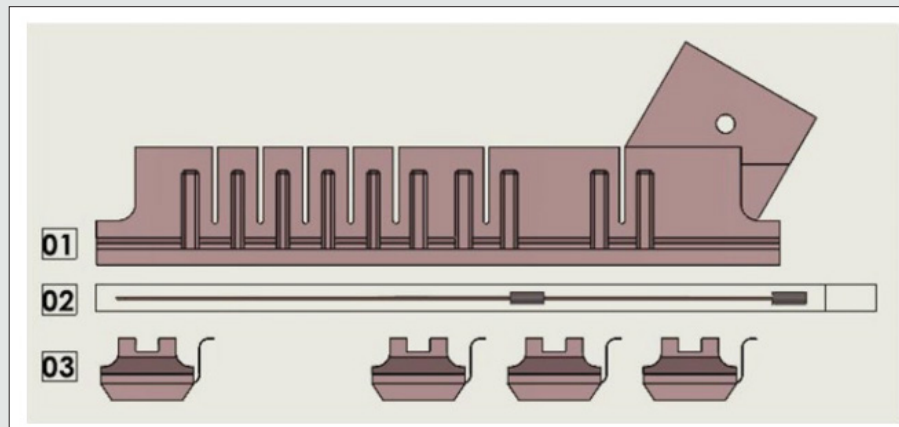
Figure 2: 3-tier actuator design.

a)   Tier 01: Uni-directional PneuNet Actuator

Similar to traditional uni-directional bellow-type PneuNet actuators [14], the actuator design utilized by this end-effector consists of a mono-pressurized, bellow-construction chamber network. However, unlike most PneuNet actuators that feature consistent incremental chamber geometry, the chamber geometry in this actuator differs mainly in two sections. As can be referenced by Figure 3, section 01 contains three larger chamber blocks of length 15.91 mm, 24.38 mm, and 21.73 mm. Internal to these three blocks are five deformable chamber walls, each with a wall thickness of 2.16 mm. In section 02, there are a total of five chamber blocks. Four of the blocks have a length of 7.45 mm while the fifth block has a length of 14.45 mm. Internal to these five blocks are a total of nine deformable chamber walls, each with a wall thickness of 2.54 mm. Chamber length and chamber wall thickness are the most critical design features of this Pneu Net actuator. The custom chamber-length layout allows for the actuator to exhibit closed-grip curvature similar to a point-finger, precisely mimicking how a finger's closed-grip trajectory wraps into itself, rather than how traditional PneuNet actuators exhibit more spherical continuous curvature deformation [15]. The difference in chamber wall thickness between sections 01 and 02 Figure 3 allows for the actuator to exhibit a more favorable motion sequence of grip. The chamber wall thickness in section 01 is roughly 380 μm less than the chamber wall thickness in section 02. Thus, when pressurized the actuator will begin to deform in section 01 before it deforms in section 02. This produces a more suitable wrapping- grip motion, rather than causing the actuator to form a closed grip pre-maturely which happens if the wall thickness is maintained evenly in both sections 01 and 02.
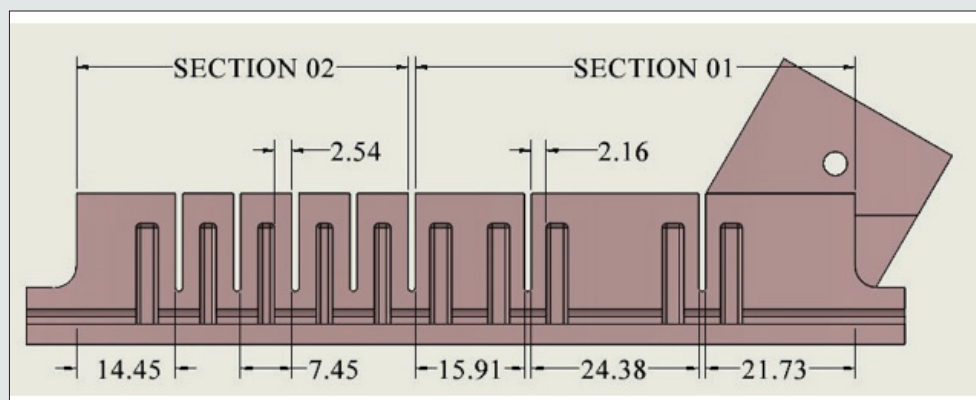

Figure 3: Uni-directional PneuNet Actuator: Varying chamber wall thickness and non-uniform chamber layout, dimensions are in mm.

b)   Tier 02: Shape Sensing Layer

In the shape sensing layer of the actuator, two piezo-resistive flex sensors are potted in 10A durometer silicone and are offset to produce a 2-part compound radius of curvature. As should be understood by Figure 4, the positioning of the flex sensors in silicone molding is capable of approximating the curvature of a close-grip pointer finger. Flex sensors are labeled as S1 and S2 accordingly. While introducing a more complex array of flex sensors would allow for more detailed curvature approximation, visual analysis of the closed-grip pointer finger depicts that its orientation can be approximated with only two flex sensors. This simplifies the numerical model needed to reproduce finger curvature while tailoring to the use of the manufacturer's smallest available off-the-shelf flex sensor inside of small spatial constraints.
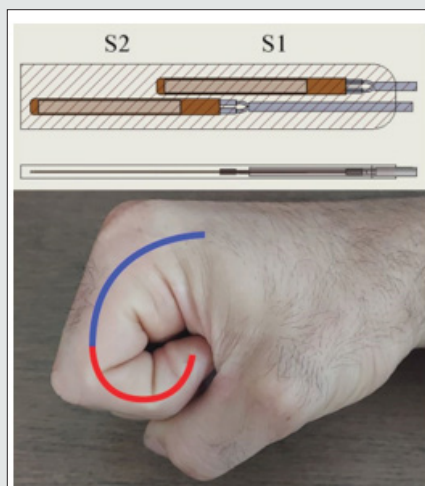

Figure 4: Flex sensor positioning: Sensors S1 and S2.

c)   Tier 03: Force Sensing Layer

Each single-point force sensor is individually potted inside of a 10A durometer silicone pad. As can be seen by Figure 5 and referenced to Figure 2, the pad features a filleted design that minimizes the surface contact between the pad bonding surface with the shape sensing layer. The idea is that the amount of bending stress transmitted to a force sensor through bending deformation of the actuator is minimized when the actuator experiences large amounts of curvature. The longitudinal shallow channel on top of the pad is used for wire-routing of successive force sensors back to the palm center of the end effector. Pads are numbered as 1, 2, 3, and 4 in each actuator according to Figure 5.
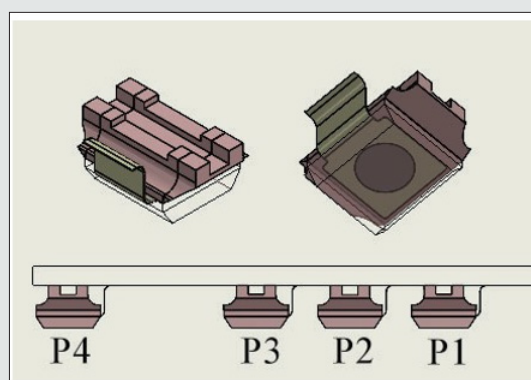

Figure 5: Force sensor pad design: Potted sensors P1, P2, P3, and P4.

Modular Front-loaded Actuator Mounting and Spline-enabled Bearing Block Interface

The end-effector features a modular front-loaded design scheme which allows for quick interchange- ability of actuators and servo units should they need to be replaced or serviced in a short time. As can be referenced by Figure 6, the end-effector's actuators are compartmentalized as their own sub-assembly, each containing a servo motor and bearing block. Figure 6(i) shows one fully assembled unit as it would be removed from the 3-digit end-effector. Figure 6(ii) conveys how the PneuNet actuator sits within

its mounting block atop the bearing block. The actuator mounting block to bearing block interface engages via a male-to-female spline connection made possible by an internal shaft central to the bearing block. This shaft allows for secure mounting of an actuator, yet quick interchangeability. Figure 6(iii) conveys the internal assemblage of the bearing block which provides a better view of the splined shaft. This component is design-critical for rotary movement transmitted from a servo to an actuator. Similar to how the actuator mounting block engages with the bearing block from above via a male-to-female spline connection with the central shaft, the servo motor engages with the central shaft from below via a male-to-female

spline connection. Thus, servo motors are also easily removable. The forward-thinking behind this front-loaded design scheme is towards future design iterations where the end-effector will be used for undersea applications that require higher pressurization. While the servo motors are waterproofed to roughly 1 m, their axial-rotational behavior is replicable of motor drives that can be encased within a pressure housing. The pressure housing would theoretically sit behind the bearing blocks and interface with the central shaft via similar male-to-female spline geometry. Therefore, the front-loaded design approach allows for compartmentalization and serviceability in the long term.
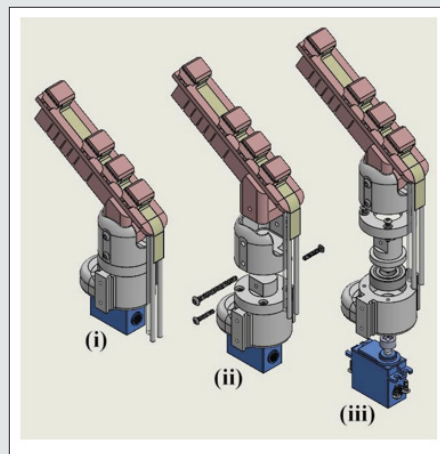

Figure 6: Actuator - Bearing Block - Servo assembly.

Force Sensor Calibration

A quality inspection was implemented to verify the sensing accuracy of each of the force sensors. A range of incremental mass, ranging from 10 grams to 400 grams, was applied to each of the force sensors. By logging the data from three consecutive rounds

of physical mass inspection, force sensor outputs (blue solid line), their standard deviation (shaded gray area), and a linear fit (orange dashed line) are plotted for calibration as seen in Figure 7. It is important to note that there is a small amount of residual fluctuation in sensor output. Thus, as applied forces were increased the deviation in voltage readings increased as well.
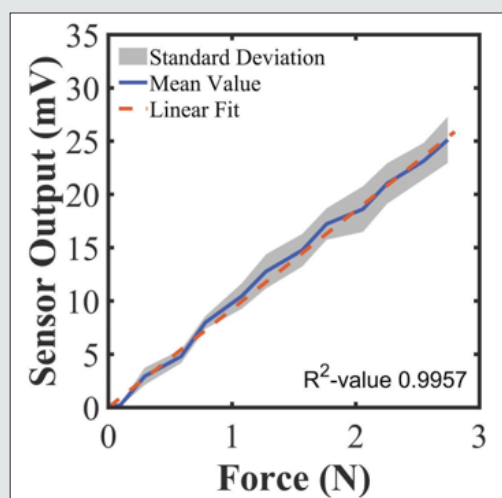

Figure 7: Graphical representation of force sensor calibration.

Shape Sensing Technique

As previously stated, the shape sensing layer of the actuator utilizes an array of two piezo-resistive flex sensors to approximate a 2-part compound radius of curvature. Each flex sensor had a slight variation in resistance range so it was necessary to compute a specific resistance-to-radius mapping for each individual sensor used. Therefore, in approximating the curvature data of an actuator the voltage outputs from each of the two embedded flex sensors were recorded seconds and converted into resistance values at intervals of 1 second within a time span from 0 to 33. Over the 33 seconds, the actuator was operated from open position to closed position. Simultaneously, camera vision was utilized to gather time-stamped images of the physical actuator curvature at each 1-second interval. A secondary drawing tool was then used to evaluate each 1-second image and measure the sizes of the two radii as shown for example in Figure 8(i).
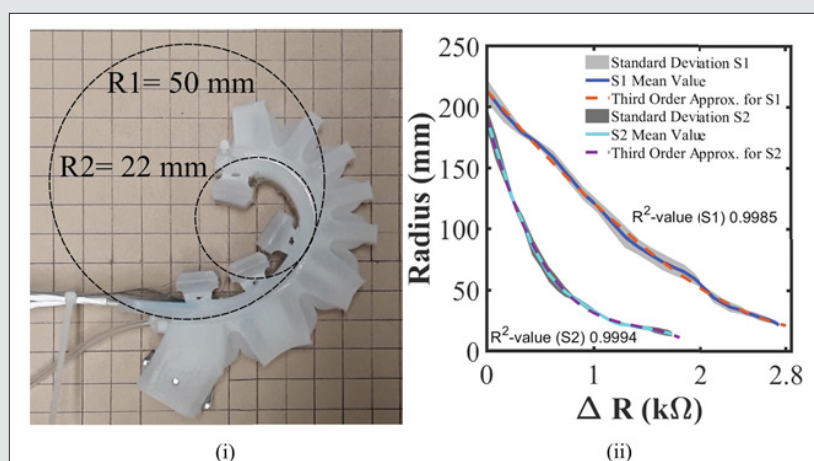

Figure 8: Calibration procedures: (i) evaluating physical radius with secondary drawing tool and (ii) graph representing change of flex sensor resistance output with the variation of radius.
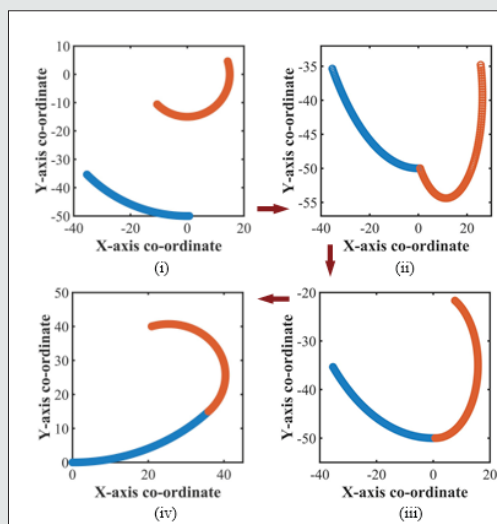

Figure 9: Representation of the algorithm to regenerate the shape of the finger.

Four full range of motion trials were performed, where flex sensor readings were logged synchronously with physical radius measurements derived from the time-stamped images and the mean value and the standard deviation are evaluated from those data. The collected dataset from the four trials is shown in Figure 8(ii) to ensure repeatability of the curvature approximation. The mean value radius outputs remained quite consistent. The S1 and S2 datasets were curve-fitted to third-order polynomial equations exhibiting R2-value of 0.9985 and 0.9994, respectively. This step was of critical importance as it generated a unique calibration equation for each flex sensor. An algebraic manipulation [16] was used to conjoin and configure a 2-part complex radius about an origin in a 2D plot. Once the calibration equations are found, they are set in MATLAB to generate the radius value from the change in resistance. Next, two simple radii of curvature are plotted with the radius values. Then, they are combined with the help of co-ordinate

transformation and made the initial portion of the S2 curve tangent to the end portion of the S1 curve. Now, the initial point of the S1 curve is set to the origin (in 2D case), or hinge point (in 3D case) and made tangent to the horizontal axis to represent the shape of the finger. The algorithm to reproduce the shape is demonstrated step by step in Figure 9. Furthermore, by superimposing time-stamped approximated curvature onto the corresponding physical

configuration of the end-effector, the shape estimation accuracy can be inspected visually. In Figure 10(ii), data comparison is shown at times of 3, 15, and 30 seconds over the 33 seconds of an entire grasping motion. As will follow in the results section is a more detailed comparison of physical configurations versus curvature approximations in the full range of motion.
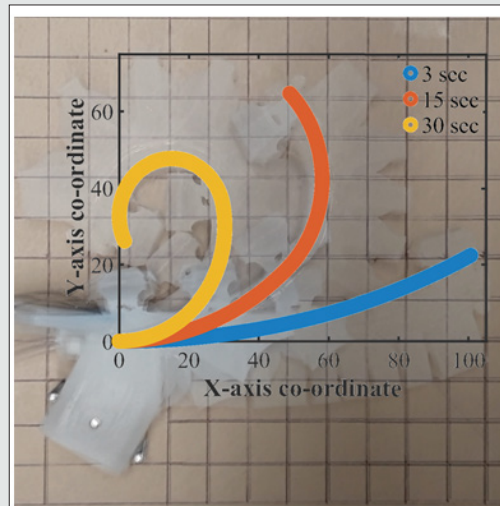

Figure 10: Comparison of physical configurations with shape estimations.

Results and Discussions

Single Actuator: Shape Sensing Performance

To experimentally verify the actuator's shape sensing performance, approximated curvature was reconstructed from the actuator's full range of physical motion and then visually compared. Figure 11 provides a detailed visual of the actuator's physical range of motion when operated from open position to closed position. Video-frame data was collected every second over 33

seconds, whereas the visual data evident in Figure 11 is provided at 3 seconds intervals to condense information. It should be noted that in comparison to Galloway et al.'s bellow-type actuators used for deep-sea reef sampling, the actuator presented in this study appears to exhibit a tighter closed-grasp curvature position [11]. More specifically, the actuator's finger-tip wraps into its own grip over the time sequence rather than deforming with continuous spherical curvature as seen with more typical bellow-type actuator designs [10-15]. This motion sequence is more comparable to how the grasping mechanics of a human pointer finger works.
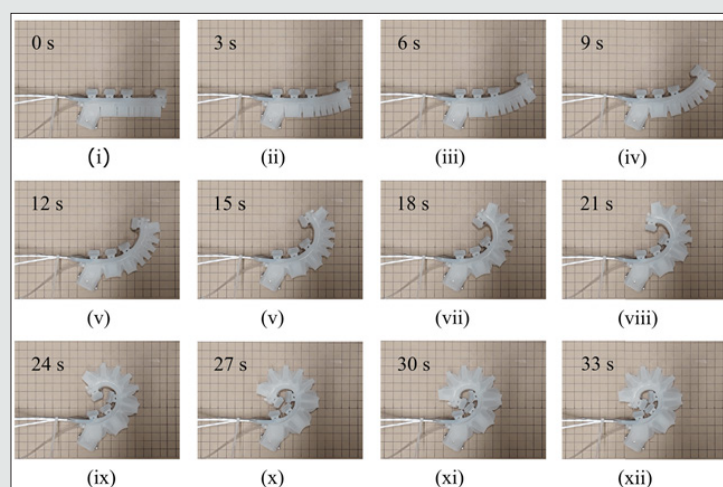

Figure 11: Physical configurations of the single actuator over the entire range of motion (0 to 33 seconds).

By applying the shape sensing algorithm to the physical range of motion the reconstruction of approximated curvature is seen to be comparable in Figure 12. It is to be mentioned that the zero-second figure was plotted manually (assuming two radius data far greater than the usual) since the radius would be theoretically infinite in that case. The consistency of the approximated curvature provides promising evidence that this approach could be implemented in future fieldwork as an accurate and effective solution to tactile undersea shape sensing. Current efforts in shape sensing for soft robotics are achieved via computation of continuum mechanics numerical models [10,11]. The shape sensing method provided in this study, based upon the reconstruction of a simplified two-part compound radius, offers an alternative approach to shape sensing through sensor measurements via the embedded piezo-resistive flex-sensor array. Of particular interest would be to integrate this simplified shape-sensing package onto existing soft-robotic end-effectors. In Galloway elal's 4-digit end-effector design, a spongy-material is mount- able to the interior grabbing surface of each actuator to facilitate toward a more pliable grasp [11]. It is realistic that the potted flex-sensor array used in this study could be similarly interfaced with designs like Galloway's without additional difficulty.
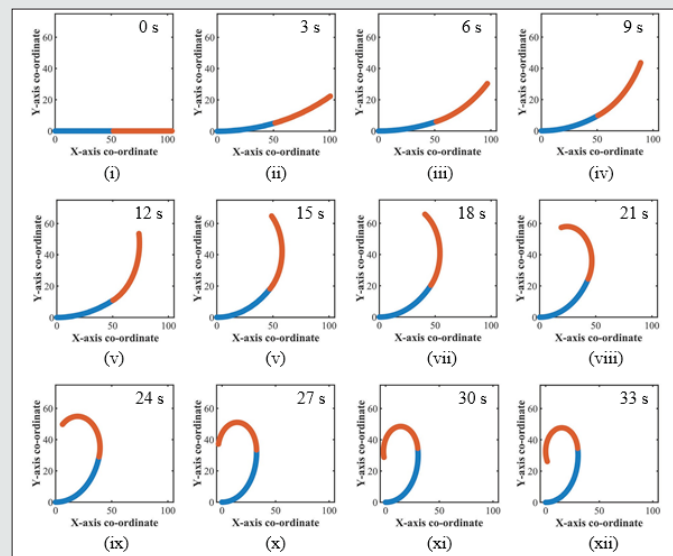

Figure 12: Estimated configurations of the single actuator (0 to 33 seconds).

Single Actuator: Force Sensing Behavior

To experimentally verify the actuator's force-sensing capabilities a transient-mode pressure test was performed on a single actuator and force contact data was logged when grasping objects. A total of six grasp trials were performed on three circular profiles of 12.5 mm - 37.5 mm radius range and two square profiles of side lengths 25 mm and 50 mm. The internal pressure of the actuator was operated through a range of 0 to roughly 73 kPa, where the actuator's initial position was the steady-state open position at 0 kPa and the actuator's final position was a firm grasp of each object at roughly 73 kPa. The time duration of each grasp trial was 50 seconds in length, and contact force data from each of the actuator's single-point force sensors were logged versus time. Figure 13 provides a visual of the final-position grasps exhibited in each of the six trials. It should be noted that two successive grasps were performed on the 50 mm side-length square in different orientations. To visualize the force-feedback data exhibited in each of the trials, Figure 14 provides the force-sensor readings over the 50 seconds time span. It should be noted that force sensors are referenced as P1, P2, P3, and P4 according to Figure 5. Therefore, images labeled (i)-(vi) are paired by the trial test with force data labeled (i)-(vi).

By comparison of the force data from each trial test with the associated grasp images, there appears to be a common trend in the data analysis. First of all, in each trial's final grasp position the force sensor pads that are visibly engaged with the objects exhibit non-zero force values. This speculation provides strong evidence that the force sensors are in fact yielding appropriately placed force-contact locations, in other words meaning that the force sensing data is reputable of which sensor pad is engaged with the object as visually supported in Figure 13. Furthermore, the positive spike in slope that appears from each actively engaged sensor pad indicates that at some variable point in time a particular sensor pad came into contact with the object under trial. Deriving information from this positive spike, it may be possible to define a force-contact thresh-hold differential based upon object material properties, whereas spikes in force-feedback that exceed the thresh-hold differential would be indicative of object contact. Thus, the actuator's curvature could be recorded as a radius snapshot in time with respect to the force-differential to provide a contact-point curvature measurement. This could prove to be an effective strategy to achieve object-shape recognition. As a point of concern, it should be noted that trial (vi) did not yield consistent results with the other five trials. More precisely, in this trial sensor pad

P4 did not exhibit a larger contact force as evident in each of the other grasp cases. This is due to minimal contact made with the single- point force sensor's active sensing area as seen in Figure 13(vi). Therefore, continued design modification to sensor pad P4 could help to reduce the sensor pad's surface area while optimizing engagement with force-sensor P4's active area.
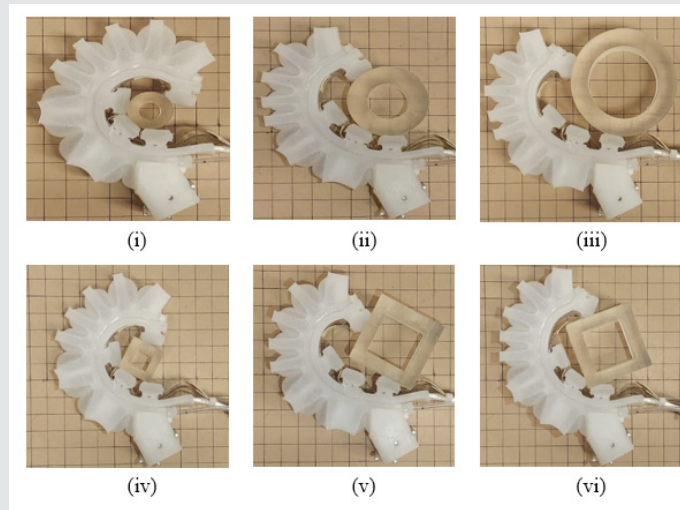

Figure 13: Single actuator grasp: Circle with radius of (i) 12.5 mm (ii) 25 mm (iii) 37.5, Square with side of (iv) 25 mm (v) 50 mm (vi) 50 mm.
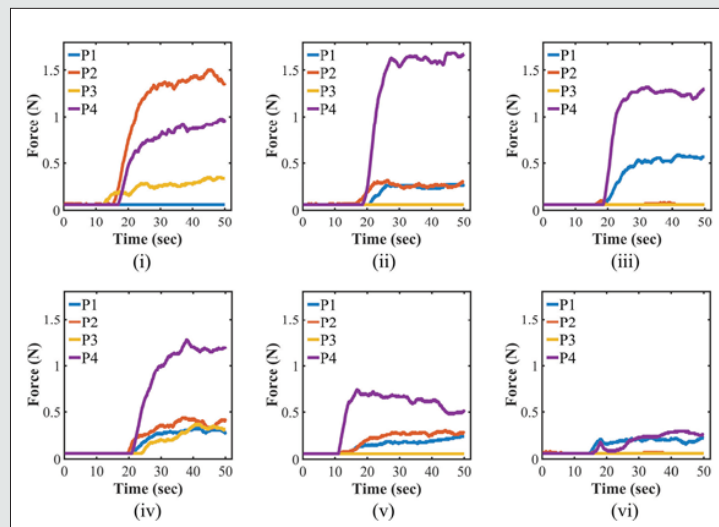

Figure 14: Contact force measurements while grasping: Circle with radius of (i) 12.5 mm (ii) 25 mm (iii) 37.5 mm, Square with side of (iv) 25 mm (v) 50 mm (vi) 50 mm.

Moving forward, the next point of interest is a visual inspection of force-feedback during trial (v). It should be noted that there is a downward trend in slope versus time after sensor pad P4 came into contact with the object. This phenomenon was observed due to shear force. As the sensor pad P4 closed its grasp onto the 50 mm-sided square it experienced a slippage. Therefore, while slipping, there was a reduction in the normal force exhibited via solid contact. As a result, there was a negative slope trend in the normal force. In this stage of the actuator technology, it is impossible to tell which direction frictional slipping is occurring, though it does seem possible to detect some amount of shear slipping. In comparison to the work presented by Kurumaya et al. and Galloway et al. though this study provides one of the first implementations of force sensor measuring equipped to bellow-type soft robotic actuators that could be outfitted for underwater use [10,11]. Finally, in trial (v) the sensor pad P2 exhibited a small amount of residual force non-indicative of the final grasp. This was either due to a non-recovering material hysteresis in the silicone which was not observed in any other trial or from some pulling stress put on sensor pad P2 from the shear forces on sensor pad P1.

Dual Actuator: Grasping Modes

The next experimental test implemented was a dual-actuator grasp test used to analyze three main grasping modes exhibited by two actuators working in tandem. It should be noted that the dual actuators were dimensionally separated as reflective of parallel orientation when mounted to the geometry of the 3-digit end-effector. The test was performed over transient internal pressure ranges, whereas the maxi- mum internal pressure of each actuator was dictated by the secure grasp of an object. A total of 11 grasp trials were performed upon four circular profiles ranging from 12.5 mm to 50 mm radius, as well as three square profiles ranging from 25 mm to 75 mm side length. In support of the grasp trials, Figure 15 provides visual proof of three main grasping modes exhibited by dual-actuator mechanics. The first grasping mode, as made evident by Figure 15(i) and Figure 15(vii), exhibits mechanics for firmly grasping smaller objects. A primary actuator is used to secure the smaller object while a secondary actuator is used to keep the primary actuator firmly closed. The second grasping mode, as made evident by Figures 15(ii)-(ix), exhibits how a secondary actuator can press a medium-sized object into the grasp of a primary actuator. In this mode of grasping, notice how the primary actuator remains slightly more open in curvature, whereas the secondary actuator exhibits tighter curvature to press the object firmly into the primary actuator's grasp. It should be noted that the pressing motion of the secondary actuator in this grasp would transmit a higher force concentration to an object, rather than distributing forces evenly throughout the engaged actuator sensor pads. The third grasping mode, as made evident by Figures 15(iv)-(xi), exhibit how both actuators can be operated with symmetrical curvature to secure the similar-sized objects to grasp mode two, however in this grasp mode force is more equally distributed between the actuators resulting in lower force concentration.
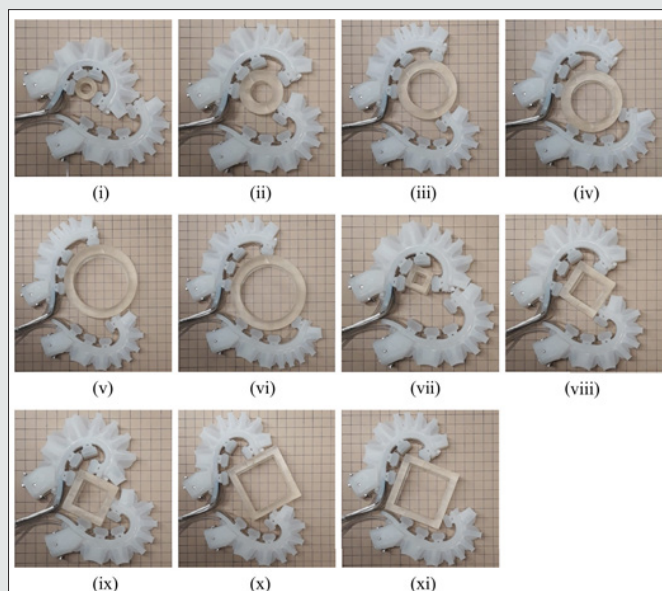

Figure 15: Dual-actuator grasps: Circle with radius of (i) 12.5 mm rad (ii) 25 mm (iii) 37.5 mm (iv) 37.5 mm (v) 50 mm (vi) 50 mm, Square with side of (vii) 25 mm (viii) 50 mm (ix) 50 mm (x) 75 mm (xi) 75 mm.

Tri-Actuator: Shape Reconstruction and Object Grasping

The experimental test implemented in this section exhibits the ability to approximate physical shape orientation for three actuators mounted together onto the 3-digit end-effector. The actuators were positioned in a parallel configuration and pressurized to various steady-state degrees of curvature as is evident by Figure 16(i). Following the shape sensing algorithm, the shapes of each actuator were approximated and plotted in 3D pertaining to the end-effector geometry. As is evident by Figure 16(ii), the 3D graph pro- vides a comparable reconstruction of the physical phenomena for actuator orientation. Therefore, the proposed curvature approximation method developed in this study seems to be an effective method for 3D-shape reconstruction and shape recognition. Figure 17 provides a visual of the 3-digit end-effector performing preliminary vertical grasps on spherical and cylindrical objects. It should be understood that force sensor data was not collected during this sequence of grasps considering that the effects due to residual object weight would disrupt the consistency of contact force measurement. Therefore, these images only provide a frame of reference to visualize the end-effector in its 120° offset configuration and parallel configuration grasping spherical and cylindrical-shaped objects. To accurately measure the multi-modal sensing capabilities of the end-effector, a waterproof test should be performed on objects of neutral buoyancy where force-contact data is logged.
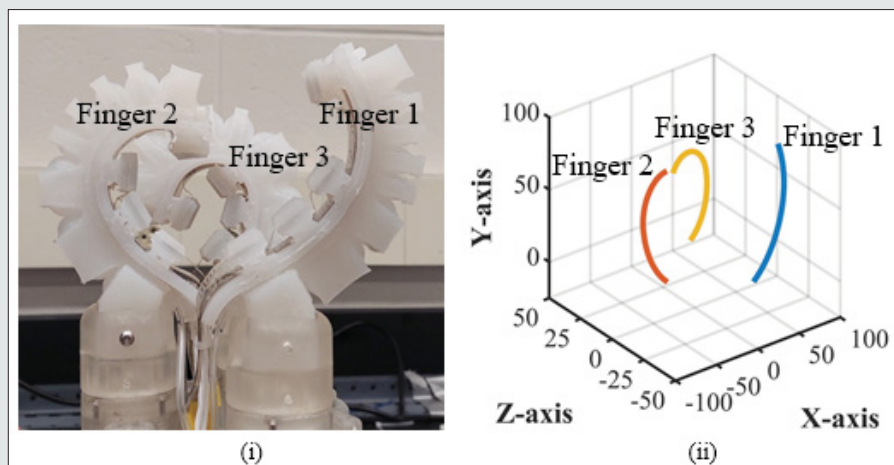
Figure 16: Tri-actuator: (i) an actual configuration (ii) 3D graphical reconstruction of the shape of 3 fingers.
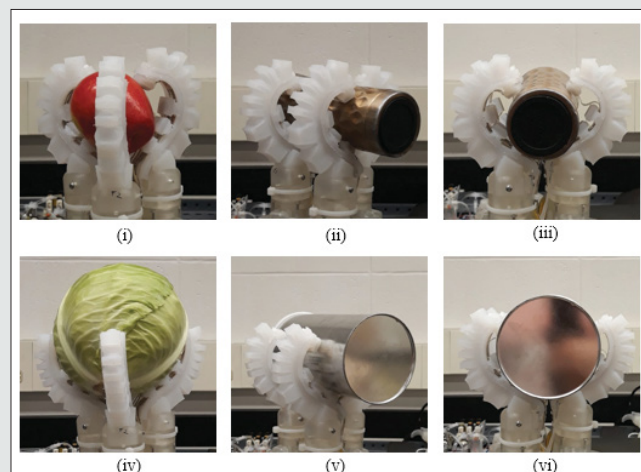

Figure 17: End-effector, three finger grasps: (i) apple, 37.5 mm radius (ii, iii) cylinder, 35 mm radius (iv) cabbage, 75 mm radius (v, vi) cylinder, 50 mm radius.

Waterproofing

To verify that all electrical connections were waterproofed in the end-effector design, it is important to perform a water-based ground-fault test on each actuator and servo unit. A ground-fault test is a basic resistance test to verify that there are no electrical shortages through the water. As can be seen by inspection of Figure 18, the component under test is submerged within water, whereas a multi-meter is utilized set to its resistance setting. The positive probe of the multimeter is incrementally connected to each of the components running wire-ends while the negative probe is electrically connected with the water. The goal of the ground-fault test is to maintain infinite resistance (OL, as displayed on a Fluke multimeter) when probing each of the wire-ends. If any numerical value other than OL displays while probing a wire, then there is exists a gap in waterproofing with regard to the potting of that specific electrical unit. It should be noted that the ground-fault test conducted in this study was performed under a depth of 250 mm of water. Thus, the test acts strictly as a preliminary waterproof test without the influence of added depth pressure based upon the test guidelines it appeared that each actuator and servo motor passed ground-fault inspection. In other words, each component was fully waterproofed allowing for the end-effector to be submerged fully within the water. As can be seen in Figure 18 the end-effector was fully submerged in water where it performed a tri-actuator grasp on a cylindrical object. While this visual only acts as a first glance into the underwater operation of the end-effector, it provides evidence of the end-effector's successful performance in the underwater domain. Therefore, future studies should be carried out to characterize the end-effector's quality of shape sensing and force sensing underwater.
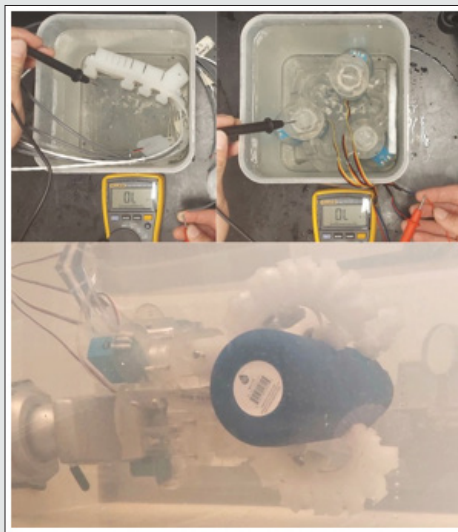
Figure 18: Ground fault testing and submerged end-effector.

Conclusions

To summarize the quality of information presented in this design review there is a clear distinction that the methods implemented for shape sensing, force sensing, and waterproofing yield verifiable and repeat- able results. In the typical scope of underwater soft robotic design, shape sensing is usually derived from continuum mechanics numerical modeling [10,11]. However, the shape sensing method provided in this study exhibits a novel and alternative approach for curvature approximation of soft robotic actuators via a cost-effective design. Successful proof of concept for force sensing provides a promising outlook that future implementation of MEMS-based force-sensing arrays will tailor to a more advanced visualization of object detection, with specific emphasis on recognizing directional shearing-force contact. Further- more, the successful fusion of waterproofed multi-modal sensing with the custom bellow-type actuator provides promising evidence that this platform for technology should be optimized for extended use in the underwater domain. Thereby motivating advancements to the area of underwater force sensing and shape sensing.

By analytically reflecting upon the actuator's grasp mechanics, visual analysis supports the addition of a finger-tip force sensor. Furthermore, the 3-digit end-effector would benefit from the addition of a palm-centered force sensing pad. Both of these design revisions would enhance the capacity for force sensing and tailor to more informed object detection and manipulation. As a future scope of work, an automated flex-sensor calibration sequence could be implemented to automatically pair flex-sensor curvature data with internal actuator pressure pertaining to pre-defined physical curvature orientation. This would significantly reduce the manual workload needed to approximate physical bend phenomena as seen in the shape sensing algorithm. Additionally, the ability to record and pair curvature data with contact force based upon recognition of force measurements that exceed some threshold values would assist toward remote object detection. Whereas the paired data could be plotted in real-time similar to how the three-actuator case was plotted in Figure 16. In closing, the presentation of technology provides a promising outlook and inspiration toward advancing underwater methods of multi-modal tactile sensing and shape recognition inside of the soft robotic framework.

References

1. Sanem Sariel, Tucker Balch, Nadia Erdogan (2008) Naval mine countermeasure missions. IEEE Robotics & Automation Magazine 15(1): 45-52.

2. Patrick Rowe (2014) A haptic sensing upgrade for the current EOD robotic fleet. In Next-Generation Robots and Systems 9116: 911602.

3. Hanns Tappeiner, Roberta Klatzky, Patrick Rowe, Jorgen Pedersen, Ralph Hollis (2013) Bimanual haptic teleoperation for discovering and uncovering buried objects. In 2013 IEEE International Conference on Robotics and Automation pp: 2380-2385.

4. George M Whitesides (2018) Soft robotics. Angewandte Chemie International Edition 57(16): 4258-4273.

5. Filip Ilievski, Aaron D Mazzeo, Robert F Shepherd, Xin Chen, George M Whitesides (2011) Soft robotics for chemists. Angewandte Chemie 123(8): 1930-1935.

6. Rafsan Al Shafatul Islam Subad, Liam B Cross, Kihan Park (2021) Soft robotic hands and tactile sensors for underwater robotics. Applied Mechanics 2(2): 356-382.

7. Marcello Calisti, Michele Giorelli, Guy Levy, Barbara Mazzolai, B Hochner, et al (2011) An octopus-bioinspired solution to movement and manipulation for soft robots. Bioin spiration & biomimetics 6(3): 036002.

8. Matteo Cianchetti, M Calisti, L Margheri, M Kuba, C Laschi (2015) Bioinspired locomotion and grasping in water: the soft eight-arm octopi's robot. Bioinspiration & biomimetics 10(3): 035003.

9. Stephen Licht, Everett Collins, George Badlissi, Domenico Rizzo (2018) A partially filled jamming gripper for underwater recovery of objects resting on soft surfaces. In 2018 IEEE/RSJ International Conference on Intelligent Robots and Systems (IROS) pp: 6461-6468.

10. Zheyuan Gong, Bohan Chen, Jiaqi Liu, Xi Fang, Zemin Liu, et al (2019) An opposite-bending-and-extension soft robotic manipulator for delicate grasping in shallow water. Frontiers in Robotics and AI 6: 26.

11. Kevin C Galloway, Kaitlyn P Becker, Brennan Phillips, Jordan Kirby, Stephen Licht, et al (2016) Soft robotic grippers for biological sampling on deep reefs. Soft robotics 3(1): 23-33.

12. Bobak Mosadegh, Panagiotis Polygerinos, Christoph Keplinger, Sophia Wennstedt, Robert F Shep- herd, et al (2014) Pneumatic networks for soft robotics that actuate rapidly. Advanced functional materials 24(15): 2163-2170.

13. Rafsan Al Shafatul Islam Subad, Liam B Cross, Kihan Park (2021) Low-Cost Shape Sensing Technique for Soft Robotic Actuators. In 2021 International Conference on Future Intelligent Computing (ICFIC), pp: 72-77.

14. Guoying Gu, Dong Wang, Lisen Ge, Xiangyang Zhu (2021) Analytical modeling and design of generalized pneu-net soft actuators with three-dimensional deformations. Soft Robotics 8(4): 462-477.

15. Yilin Sun, Qiuju Zhang, Xiaoyan Chen, Haiwei Chen (2019) An optimum design method of pneu-net actuators for trajectory matching utilizing a bending model and ga. Mathematical Problems in Engineering.

16. Isaac M Di Napoli, Casey M Harwood. Design and benchmarking of a robust strain-based 3d shape sensing system. Ocean Engineering 201: 107071.
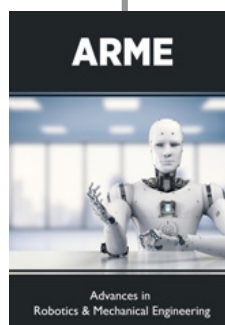
Advances in Robotics & Mechanical Engineering

Assets of Publishing with us

- Global archiving of articles
- Immediate, unrestricted online access
- Rigorous Peer Review Process
- Authors Retain Copyrights
- Unique DOI for all articles